Information content of volume holographic imaging

George Barbastathis and Arnab Sinha

We discuss the general properties of optical imaging in three-dimensional object domains from an information-theoretic standpoint, expressing system performance in terms of imaging mutual information (IMI). We use IMI to characterize volume holographic imaging, a new optical imaging method with depth discrimination capability. The performance of this holographic method in imaging a simple discrete, axial fluorescent object is compared with that of two alternatives: a pinhole-based system and a combined system that uses both a pinhole and a hologram in parallel.

The ability to acquire three-dimensional (3D) information about objects non-invasively has led to significant advances in many scientific areas over the past two to three decades. Medical imaging and bioimaging especially have benefited from these developments. For example, optical, acoustical, magnetic and radiometric imaging have been used widely in laboratories as well as in the clinic. Each method has competitive advantages in different applications or areas of interest.

Optical imaging is necessary to accomplish spatial resolution of the order of a few micrometers, but it can be used successfully only on objects with small absorption and scattering coefficients at visible wavelengths. Assuming that absorption and scatter do not present problems, the performance of an optical imaging system is still limited by several factors, such as the capabilities of the optical elements used to construct the system, the optical power available from the object and the post-processing of the image data. In this article, Shannon's mutual information[1–4] (a well known image-performance metric) is used to model the performance of pinhole-based systems and volume HOLOGRAMS (see Glossary) (a type of imaging element that has only recently been proposed[5,6]).

The imaging of 3D objects presents a fundamental problem in that detector arrays are necessarily two-dimensional (2D). Several imaging techniques, including confocal microscopy[7,8], optical coherence tomography (OCT)[9] and coherence imaging[10–14], solve this problem by limiting the 3D field of view and scanning across the 3D object. For example, a confocal microscope at any given time acquires a point (zero-dimensional) measurement; volumetric reconstruction is obtained by scanning in 3D. The same is true for an OCT imager. A coherence imager, such as a rotational shear interferometer (RSI) can, in principle, acquire an entire 2D cross-section at once; therefore, one-dimensional scanning

George Barbastathis*
Arnab Sinha
Dept of Mechanical Engineering, Massachusetts Institute of Technology, Rm 3-461c, 77 Massachusetts Ave, Cambridge, MA 02139, USA.
*e-mails: gbarb@mit.edu and arnab@mit.edu

Glossary

Bragg matching: The set of conditions that must be met in order to obtain significant diffraction from a volumetric structure, such as a volume hologram. A probe beam with identical wavelength and angle of propagation to that of the reference beam is automatically Bragg matched.

Diffraction: Caused by the wave nature of light as the light propagates around or through objects with sharp or small features. Both sharpness and size are determined by comparison with the optical wavelength. Holograms also diffract light to produce holographic reconstructions.

Entropy: A measure of the uncertainty associated with a random variable. Uncertainty also measures the information content of the answer to a question. This can be understood by comparing two questions.

(1) Did you win the lottery yesterday?

(2) Did the coin toss result in a head?

Both receive a 'yes/no' answer but answering the first question with a 'no' is fairly certain to be correct. However, the answer to the second question is completely uncertain for a fair coin. Information theory shows that the coin question has higher entropy than the lottery question.

Information is measured differently for discrete and continuous random variables. For discrete random variables (the coin toss for example), the information is measured in bits. The answer to the coin-toss question is worth exactly one bit for a fair coin. The answer to the lottery question for the state of Massachusetts in the USA is worth ~2×10^{-5} bits. The information of continuous random variables (for example, light intensity at high photon counts) is measured by the differential entropy in nats (1 nat = $\log_2 e$ bits). For example, if the light intensity is a Gaussian with a mean of 1 W and a variance 0.25 W, the information content of the light intensity distribution is 0.0326 nats.

Hologram: An optical element that contains both amplitude and phase information about an object. The hologram of an object is generated by recording the interference pattern of the light scattered by the object with a coherent reference. The recording is often achieved by modulating the refractive index of a photosensitive medium.

Nat: A measure of the information content of a continuous, random variable (see Entropy).

Refractive index: The refractive index of a medium is defined as the ratio of the speed of light in vacuum to the speed of light in that medium. The refractive index of certain materials (e.g. lithium niobate, $LiNbO_3$) changes when the material is exposed to a light beam. If, instead, the material is exposed to an interference pattern (resulting from a reference and an object beam), a hologram is recorded as a modulation of the refractive index.

Three-dimensional (3D) imaging: The acquisition of the optical properties of an object (such as absorption and optical density) as function of the three spatial dimensions x, y and z. By contrast, two-and-a-half-dimensional imaging refers to the acquisition of the shape of a reflective surface as a height map $z(x,y)$.

Volume hologram: A volume hologram is a thick hologram (>50 wavelengths, as a rule of thumb). The qualitative differences between volume and thin holograms are summarized as follows.

(1) A thin hologram diffracts two beams, the forward and the so-called pseudoscopic reconstruction[a], whereas the volume hologram only diffracts the forward reconstruction.

(2) A thin hologram diffracts light under almost arbitrary illumination conditions, whereas the volume hologram diffracts only when the illumination is Bragg matched. This selectivity forms the basis of the applications of volume holograms in data storage and imaging.

Reference

a Goodman, J.W. (1996) *Introduction to Fourier Optics* (2nd edn), Section 9.4, McGraw Hill

 0167-7799/01/$ – see front matter PII: S0167-7799(01)01743-7

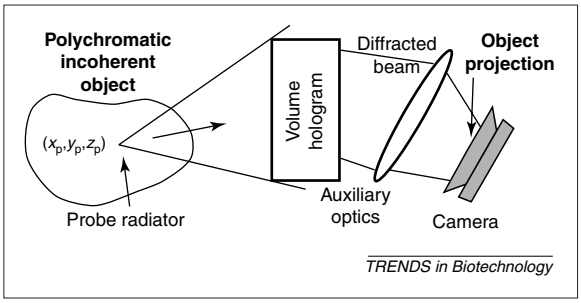

Fig. 1. The hologram is illuminated by the radiation from the object and diffracts a portion of the radiation towards a detection plane, where one or several intensity measurements are taken. The portion of the energy diffracted by the hologram is measured by its diffraction efficiency η. The undiffracted light passes through the hologram and can serve as input to another imaging system.

suffices to reconstruct the object in 3D. Typically, however, additional scans need to be acquired to reduce phase noise in the data[15].

Holograms as 3D optical elements

Recently, the use of VOLUME HOLOGRAMS (Fig. 1) as 3D IMAGING elements was proposed, first in the context of super-resolving confocal microscopy[5] and subsequently in more general contexts[6,16]. The principle of volume holographic imaging relies on the hologram being illuminated by the radiation from the object and DIFFRACTING some of the radiation towards a detection plane, where one or several intensity measurements are taken. The portion of the object radiation that is not diffracted by the hologram but instead propagates straight through the hologram can be discarded. Better yet, the undiffracted light can be used as an input to some other imaging system operating at the same time. The intensity measurements are then processed to reconstruct the intensity distribution of the object. It has been shown[6] that the information recovered from the object can span all three spatial dimensions as well as the spectral (color) dimension. Therefore, the hologram could be used to perform four-dimensional imaging. Here, however, the discussion is limited to spatial imaging in 3D only.

The object-to-image mapping properties of the volume hologram are given by the matched filter behavior of volume holograms with respect to their input illumination. This behavior is well known from the study of holographic storage and optical pattern recognition. That is, a volume hologram, unlike thin diffractive elements, diffracts selectively; of all the components of a complex illuminating beam, significant scattering is produced only by those components that yield phase-matched diffraction along the entire length of the volume hologram. This matched filtering of the field input to the hologram is achieved by BRAGG MATCHING. Bragg matching along the lateral spatial dimensions (i.e. perpendicular to the optical axis) forms the basis of image correlators[17,18] and angle- and shift-multiplexed[19,20] holographic memories. Bragg matching in the spectral dimension forms the basis of wavelength multiplexing[19].

IMI of incoherent imaging systems

In the following discussion, we assume that the object is the primary source of light distributed within the volume v_S. We also assume that the object is spatially incoherent and monochromatic. Fluorescent objects match these properties fairly accurately in practice.

Let $I(\mathbf{r})$ denote the intensity distribution of the object as function of the spatial coordinate $\mathbf{r}$ in object space (that is, $\mathbf{r} \in v_S$). After passing through an arbitrary linear optical system, the light intensity is transformed according to Hopkins' integral (Eqn 1),

$$\tilde{I}(\mathbf{r}') = \int_{v_s} h(\mathbf{r},\mathbf{r}')I(\mathbf{r})\mathrm{d}^3\mathbf{r} \qquad [1]$$

where $h(\mathbf{r}, \mathbf{r}')$ is the incoherent impulse response of the system. The output intensity $\tilde{I}(\mathbf{r}')$ is observed in an appropriate detector space, typically restricted to lie on a plane.

Eqn 1 is a Fredholm integral equation of the first kind, which are commonly encountered in inverse problems[21]. It is generally known that these problems are ill-posed, because the kernel $h(\mathbf{r}, \mathbf{r}')$ delocalizes the spatial contents of the source at the detector space. Moreover, in the case of volumetric imaging, there is a dimensional mismatch between the object and detector spaces (3D and 2D, respectively). The obvious way around the mismatch is to make the problem discrete and to make sure that there are at least as many intensity measurements available as there are desired samples from the object intensity distribution.

In this article, we will assume that the source is also discrete. This assumption is not necessary but it simplifies the estimation of imaging quality that follows, without seriously compromising the qualitative nature of the conclusions. The truth of this statement depends, of course, on the sampling scheme and, here, we will assume that the sampling has been done correctly.

To treat the discrete model, a vector $\underline{I}$ of object intensities and a vector $\underline{\tilde{I}}$ of intensity measurements are formed. (In this article, bold face is used for position vectors in Cartesian space, underscore for vectors of intensity values, such as collections of object and image samples, and underscored bold face for matrices.) The intensity measurement vector should contain all the measurements pertinent to the imaging task at hand. For example, in the case of a confocal microscope, $\underline{I}$ is formed by all the pointwise measurements. The superposition integral (Eqn 1) then becomes a simple matrix equation (Eqn 2),

$$\underline{\tilde{I}} = \underline{\underline{\mathbf{H}}}\,\underline{I} \qquad [2]$$

where element $\underline{\underline{\mathbf{H}}}_{jk}$ of system matrix $\underline{\underline{\mathbf{H}}}$ quantifies the intensity contribution of source number k, $\underline{I}_k$, to measurement number j, $\underline{\tilde{I}}_j$.

The resolution limitation of an imaging system is associated with the stability of its corresponding matrix $\underline{\underline{\mathbf{H}}}$ to inversion. For example, consider the

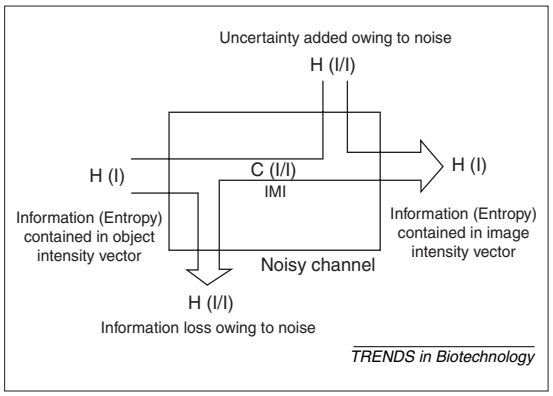

Fig. 2. The imaging mutual information (IMI) measures the actual amount of information that is obtained after transmission through a noisy channel. The IMI is a measure of the relevant information from a measurement because it disregards contributions from channel noise.

simple case of imaging two discrete point sources using a system matrix (Eqn 3).

$$\underline{\mathbf{H}} = \begin{bmatrix} 1 & \varepsilon \\ \varepsilon & 1 \end{bmatrix} \quad [3]$$

The term ε in Eqn 3 ($\varepsilon < 1$) quantifies the 'cross-talk' that each point source contributes to the measurement of its counterpart (in a typical optical imaging system, ε would increase to 1 as the distance between the two sources decreases). Suppose also that the measurement contains noise (Eqn 4),

$$\underline{\tilde{I}} = \underline{\tilde{I}}^{(O)} + \underline{\tilde{I}}^{(N)} \quad [4]$$

where $\underline{\tilde{I}}^{(O)} = \underline{\mathbf{H}}\,\underline{I}$ is the ideal image and $\underline{\tilde{I}}^{(N)}$ is the perturbation owing to noise. Inverting Eqn 3, we obtain the estimate of the object as Eqn 5.

$$\underline{I}^{(est)} = \underline{I} + \underline{H}^{-1}\underline{\tilde{I}}^{(N)} = \underline{I} + \frac{1}{1-\varepsilon^2}\begin{bmatrix} 1 & -\varepsilon \\ -\varepsilon & 1 \end{bmatrix}\underline{\tilde{I}}^{(N)} \quad [5]$$

From Eqn 5, the error owing to the noise can be seen to be amplified by $[\varepsilon \div (1-\varepsilon^2)]$ times the relative value of the noise itself. The amplification factor can grow quite large as ε tends towards 1. Thus we see that, if the two object sources are too close together (and hence ε approaches 1), the imaging inversion operation becomes unstable with respect to the noise-induced perturbation in the data. This kind of instability is characteristic of ill-posed problems. (Notice that, if $\varepsilon = 1$, the matrix becomes singular; that is, no image can then be formed.)

Several metrics exist in the literature for measuring the stability of a matrix, such as the eigenvalue spectrum[22], Fisher information[23] and the Hotelling trace[24]. In this article, inversion stability is measured using Shannon's mutual information. The justification for this choice is that, typically, the inversion operation does not end with the measurement $\underline{\tilde{I}}$. The quality of the image can be much improved by nonlinear regularization methods or various forms of statistical processing and by the use of prior information about the object. All these methods essentially attempt to separate the noise content of the measurements from the contributions of the object itself. Shannon's theory provides good estimates of the upper bound on post-processed image quality that the system can achieve.

Mutual information can be understood from Figure 2. $H(\underline{I})$ is the differential ENTROPY of the object to be imaged. In other words, $H(\underline{I})$ NATS of information are needed to answer the question 'What is the intensity of the object as a function of the spatial coordinates?' for the problem at hand. Light emitted by the object propagates, reaches the detector and forms an image. The differential entropy of the image is $H(\underline{\tilde{I}})$. In the absence of noise, $H(\underline{\tilde{I}}) = H(\underline{I})$ and so, in the absence of noise, the object and the image contain exactly the same amount of information and the imaging operation is perfect. The image is a deterministic function of the object and the object can be inferred from the image without any uncertainty.

However, the presence of noise in the channel introduces some uncertainty into the system's ability to infer the object given complete image information. This uncertainty is quantified by the conditional entropy $H(\underline{I}\,|\,\underline{\tilde{I}})$ which is the differential entropy of I given $\underline{\tilde{I}}$. In other words, the amount of useful information propagating in the imaging channel is the information contained in the object minus the uncertainty induced by the channel noise. This is illustrated in the left-hand part of Fig. 2 and is expressed as Eqn 6.

$$C(\underline{I},\underline{\tilde{I}}) = H(\underline{I}) - H(\underline{I}\,|\,\underline{\tilde{I}}) \quad [6]$$

Alternatively, one could regard the image information as the sum of the useful object information that the channel carries and some entropy added by the channel noise. This entropy quantifies the conditional uncertainty of the image given the object $H(\underline{\tilde{I}}\,|\,\underline{I})$. In this case, the useful information carried by the channel is quantified by the information content of the image minus the uncertainty added by noise (Eqn 7). (This is illustrated by the right-hand part of Figure 2.)

$$C(\underline{I},\underline{\tilde{I}}) = H(\underline{\tilde{I}}) - H(\underline{\tilde{I}}\,|\,\underline{I}) \quad [7]$$

In Eqns 6 and 7, $C(\underline{I},\underline{\tilde{I}})$ is the same quantity and is known as the mutual information of the channel. It is a measure of the information that is common between the input to and output of the channel. Hence, if the mutual information is maximized, the channel performs optimally under the constraints imposed by channel noise. In the context of imaging, $C(\underline{I},\underline{\tilde{I}})$ is referred to as the imaging mutual information (IMI).

Precise calculation of the IMI requires knowledge of the object statistics as well as the joint statistics of the object and image. Unfortunately, 3D object models in the literature

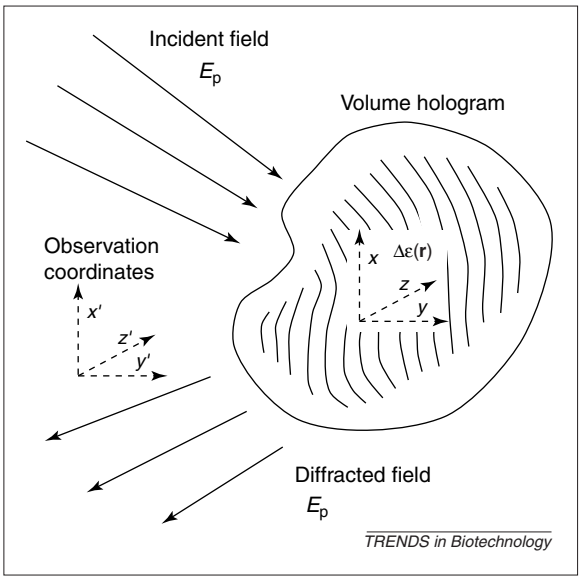

Fig. 3. Volume diffraction geometry and coordinates. Notice that the undiffracted portion of the incident beam would pass straight through the hologram.

provide up to second-order correlations, whereas calculation of the probability density function requires all orders. Moreover, the problem of determining joint statistics between object and image from the statistics of the object and the statistics of the noise is intractable for realistic noise models (e.g. Poisson). To develop a simple, tractable model, we make the following assumptions:

- the object intensity is distributed according to the Gaussian function around a mean intensity $\tilde{I}_0$ with variance σ_{obj}^2, and we might neglect the negative tail of the object distribution;
- the individual sources composing the discretized object are mutually independent (this is a stronger assumption than mutual incoherence);
- the noise is uncorrelated with the measurement and it is white, additive Gaussian noise with mean zero and variance σ^2 (this model is good for electronic noise added by the detector circuitry but models Poisson noise very poorly).

With these assumptions, and for a square system matrix $\underline{\mathbf{H}}$, the IMI can be calculated explicitly[25] (Eqn 8),

$$C(\underline{\mathrm{I}},\underline{\tilde{\mathrm{I}}}) = \sum_{n-1}^{N} \log\left(1 + \frac{\tilde{I}_0 \mu_n^2}{\sigma_{obj}^2 + \sigma^2}\right) \qquad [8]$$

where μ_n are the eigenvalues of the $N \times N$ matrix $\underline{\mathbf{H}}$. The result remains true for rectangular matrices (i.e. over- or under-determined systems) except that the singular values must then be used instead of the eigenvalues. The proofs are straightforward and will not be given here.

Intuitively, Eqn 8 is saying that the effective rank or number of degrees of freedom of the system (that is, how many measurements contribute useful information towards determining the object) is limited by the noise present in the system relative to the power emitted by the objects. In an imaging system with an ideal matrix $\underline{\mathbf{H}}$ (such as the identity matrix for objects with our assumed statistics), all measurements contribute equal amounts of information about the object (because all eigenvalues are equal). Generally, off-axis matrix elements bias the eigenvalue spectrum towards lower values, which in turn decreases the IMI.

The question then becomes: how can one design an imaging system such that the IMI is maximized under general conditions of object and noise statistics? This problem presents interesting challenges, both theoretical and practical. From the theoretical point of view, there are difficulties associated with the statistical calculations, as pointed out earlier. Assuming that this problem is solved, the next issue is to implement optical elements in practice such that the desired $\underline{\mathbf{H}}$ is achieved.

Volume holographic imaging in the transmission geometry

A volume hologram results when a thick photosensitive material is exposed to two (or more) interfering light beams. The interference pattern is recorded as small (of the order of 10^{-3} to 10^{-1}, depending on the material) local changes (modulation) in the material's REFRACTIVE INDEX. Consider the general geometry of Figure 3. If the modulation is described by the function $\Delta\varepsilon(\mathbf{r})$, the light diffracted by the volume hologram in response to an illuminating (probe) field $E_p(\mathbf{r})$ is given approximately by Eqn 9,

$$E_d(\mathbf{r}') = \sqrt{\eta}\int E_p(\mathbf{r})\Delta\varepsilon(\mathbf{r})G(\mathbf{r}'-\mathbf{r})\mathrm{d}^3\mathbf{r} \qquad [9]$$

where η is the diffraction efficiency and $G(\mathbf{r})$ is Green's function for free space (Eqn 10).

$$G(\mathbf{r}) = \frac{e^{ik|\mathbf{r}|}}{|\mathbf{r}|} \qquad [10]$$

Therefore, the diffracted field is approximated by the superposition of fields scattered by individual point radiators such that the radiation generated at each point is proportional (in amplitude and phase) to the product of the illuminating field and the local index modulation. This approximation obviously neglects rediffraction of the scattered field as it propagates through the volume hologram; this is valid only if the hologram is relatively weak (in practice, it works well for η up to 50% or even higher, depending on the specific modulation). This formulation is known as the first-order Born approximation and is used widely in volume diffraction.

Now, we can explicitly calculate the diffracted field for the case of a volume hologram acting as an imaging element, using the transmission holographic geometry of Figure 4. The holographic medium is a disk with thickness L and radius R. The hologram is recorded by the interference of a plane wave signal beam and a spherical reference beam. The reference emanates from a point source at

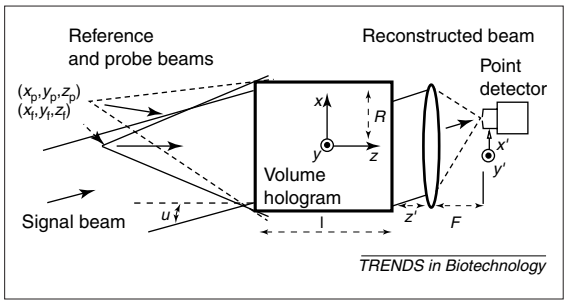

Fig. 4. Transmission geometry with spherical wave reference and plane wave signal beams.

$\mathbf{r}_f = x_f\hat{\mathbf{x}} + y_f\hat{\mathbf{y}} + z_f\hat{\mathbf{z}}$ ($\hat{\mathbf{x}}, \hat{\mathbf{y}}$ and $\hat{\mathbf{z}}$ represent the unit vectors along the **x**, **y** and **z** directions, respectively). We express this wave in the paraxial approximation as Eqn 11.

$$E_f(\mathbf{r}') = \exp\left\{i2\pi\frac{z - z_f}{\lambda} + i\pi\frac{(x - x_f)^2 + (y - y_f)^2}{\lambda(z - z_f)}\right\} \quad [11]$$

Notice that in Eqns 11 and 12, a term of the form $1 \div [\lambda(z - z_f)]$ is neglected because it varies with z much more slowly than the exponential term. The signal beam is a plane wave propagating at an angle θ that is $\ll 1$ with respect to the $\hat{\mathbf{z}}$ axis. In the paraxial approximation, it is expressed as Eqn 12.

$$E_S(\mathbf{r}) = \exp\left\{i2\pi\left(1 - \frac{\theta^2}{2}\right)\frac{z}{\lambda} + i2\pi u\frac{x}{\lambda}\right\} \quad [12]$$

After recording is complete, the index modulation recorded in the hologram is given by Eqn 13,

$$\Delta\varepsilon(\mathbf{r}) \propto E_f^*(\mathbf{r})E_S(\mathbf{r}) \quad [13]$$

where the asterisk denotes a complex conjugate. The actual interference pattern is given by $|E_f + E_s|^2$ but, of the four resulting product terms, only the one in Eqn 13 results in significant diffraction (the remaining three terms are Bragg mismatched).

Given that the object is discretized in this formulation, it suffices to calculate the intensity response of the volume hologram to individual point sources at arbitrary spatial coordinates. The intensity collected at any individual point in the detector plane is then given simply by the sum of the intensities contributed by the corresponding diffracted fields, which is consistent with the incoherent object assumption (Eqns 1, 2, 23). Consistent with the notation used before, the object samples are indexed by k, where $k = 1 \ldots N$, where N is the number of samples.

Source number k probing the volume hologram is modeled as a spherical wave at the same wavelength λ as the reference. The wave is emanating at $\mathbf{r}_{p,k} = x_{p,k}\hat{\mathbf{x}} + y_{p,k}\hat{\mathbf{y}} + z_{p,k}\hat{\mathbf{z}}$. The expression for the probe field is given by Eqn 14,

$$E_p(\mathbf{r}) = \sqrt{I_k}\,\exp\left\{i2\pi\frac{z - z_{p,k}}{\lambda_p} + i\,\pi\frac{(x - x_{p,k})^2 + (y - y_{p,k})^2}{\lambda_p(z - z_{p,k})}\right\} \quad [14]$$

where I_k represents the intensity emitted by source number k. The diffracted field is observed at detector coordinates $\mathbf{r}'$ on the focal plane of the Fourier-transforming lens (Fig. 4). Taking Eqn 9 with Eqns 11–14 and Fourier-transforming the result[26] gives Eqn 15.

$$\tilde{E}_d(\mathbf{r}') = 2\pi R^2\sqrt{\eta I_k}\int_{-L/2}^{L/2}\exp\{i\pi C(z)\}\,\mathrm{L}(2\pi A(z)R^2, 2\pi B(z)R)dz \quad [15]$$

The coefficients $A(z)$, $B_x(z)$, $B_y(z)$ and $C(z)$ are given by Eqns 16–20.

$$A(z) = \frac{1}{\lambda(z - z_f)} - \frac{1}{\lambda(z - z_{p,k})} \quad [16]$$

$$B_x(z) = -\frac{x_{p,k}}{\lambda(z - z_{p,k})} + \frac{x_f}{\lambda(z - z_f)} - \frac{x'}{\lambda F} + \frac{\theta}{\lambda} \quad [17]$$

$$B_y(z) = -\frac{y_{p,k}}{\lambda(z - z_{p,k})} + \frac{y_f}{\lambda(z - z_f)} - \frac{y'}{\lambda F} \quad [18]$$

$$B(z) = \sqrt{B_x(z)^2 + B_y(z)^2} \quad [19]$$

$$C(z) = \frac{x^2_{p,k} + y^2_{p,k}}{\lambda(z - z_{p,k})} - \frac{x_f^2 + y_f^2}{\lambda(z - z_f)} + \left(\frac{x'^2 + y'^2}{\lambda F^2} - \frac{\theta^2}{\lambda}\right)z \quad [20]$$

Eqn 21 is the same integral that occurs in the calculation of the 3D light distribution near the focus of a lens (in this equation ρ is the variable of integration)[27].

$$f(u, v) = \int_0^1 \exp\left\{-\frac{i}{2}u\rho^2\right\}J_0(v\rho)\rho\,d\rho \quad [21]$$

The intensity contributed by the probe source to the detector plane is represented by Eqn 22.

$$\tilde{I}_k(\mathbf{r}') = \left|\tilde{E}_d(\mathbf{r}')\right|^2 \quad [22]$$

The total intensity $\tilde{I}(\mathbf{r}')$ is the sum of all the contributing point sources (Eqn 23).

$$\tilde{I}(\mathbf{r}') = \sum_{k=1}^{N}\tilde{I}_k(\mathbf{r}') \quad [23]$$

The result for the diffracted field (Eqn 15) has an interesting interpretation based on the nature of the function $f(.,.)$. The volume hologram can be decomposed into infinitely many successive thin lenses stacked along the $\hat{\mathbf{z}}$ direction. Each lens

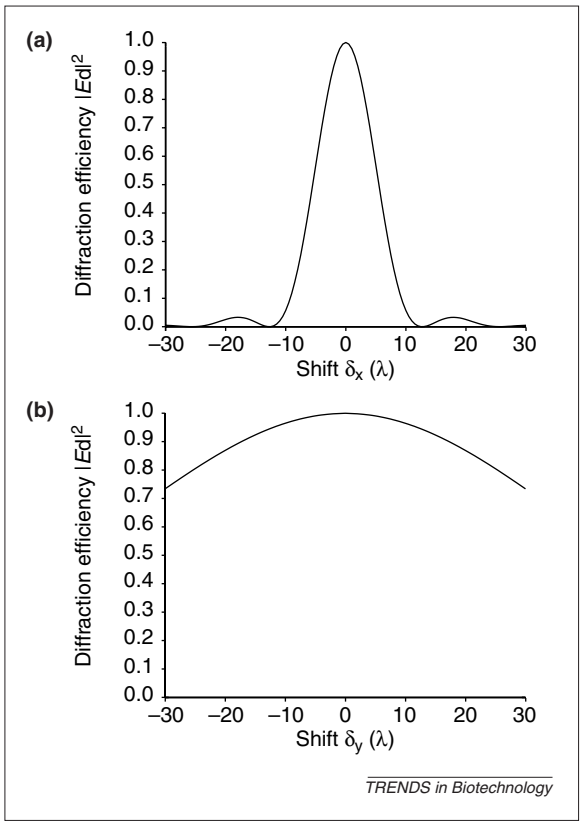

Fig. 5. Dependence of the intensity diffracted by a volume hologram towards the focal point for displacements along (a) *x* and (b) *y* directions. The calculation used $\mathbf{r}_f = (0, 0, -10^4\lambda)$, $u = 0.2$, $R = 500\,\lambda$, $l = 4 \times 10^3\,\lambda$.

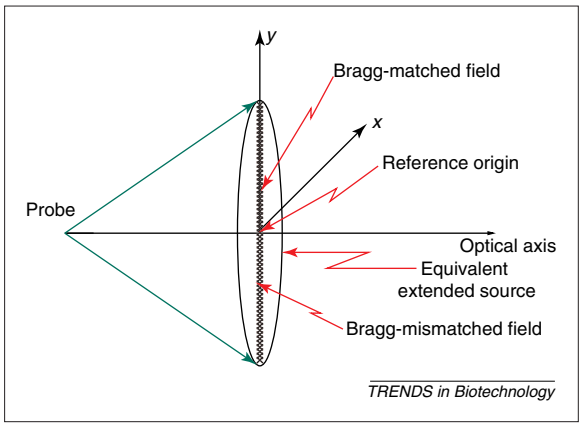

Fig. 6. Probe source displaced in the longitudinal direction with respect to the reference (*x*–*y*) plane. The field produced by the probe is equivalent to an extended source located at the reference plane. According to the discussion of lateral displacement, the only portion of the equivalent extended source that is Bragg matched is a thin strip along the *y* axis. The remainder of the extended source is Bragg mismatched, resulting in an overall drop in the diffracted intensity compared with that for the exactly Bragg-matched probe location ($\mathbf{r}_{p,k} = \mathbf{r}_f$).

produces an elemental diffracted field and the total volume-diffracted light is the coherent superposition of all these individual fields. If the probe source is at the common front focus of all these virtual lenses then the individual lens fields are all in phase and give a strong reconstruction in the back focal point (Bragg matching). If the probe is at a different location, contributions from the lenses are, in general, out of phase, resulting in Bragg mismatch, and the reconstructed amplitude drops. The only exception is if the probe location has the same *y* coordinate as the reference origin $\mathbf{r}_f$ (i.e. if $y_{p,k} = y_f$), in which case the probe remains approximately Bragg matched and diffracts with almost equal strength. The intensity diffracted towards the focal spot as function of probe displacement relative to $\mathbf{r}_f$ in the two orthogonal directions *x* and *y* is compared in Figure 5.

Even richer behavior is obtained if the wavelength of the probe source is not λ (Refs 6,28). These properties are of interest for spectrally resolved volumetric imaging; that is, for imaging in four dimensions (three spatial and one spectral). However, a detailed description of the coupling between probe wavelength, location and Bragg matching is beyond the scope of this article.

According to volume diffraction theory, the behavior of the hologram in response to probe displacement is asymmetric in the two lateral directions. The hologram behaves like a lens in the *y* direction but, in the *x* direction, it acts as a pinhole: if the probe is displaced in that direction, the diffracted beam is vignetted out by Bragg mismatch. Therefore, the volume hologram is actually shift invariant in the *y* direction and shift variant in the *x* direction. This property is well known[18] and has formed the basis of many optical pattern-recognition systems in the past[17].

The partial shift variance of volume holograms was exploited in Ref. 5 for depth-selective imaging. The behavior of the diffracted field as a function of longitudinal probe displacement can be explained in terms of its behavior for lateral displacements, which we have already discussed (Fig. 6).

IMI for fluorescent objects elongated in the direction of the optical axis

Consider an object modeled as *N* mutually incoherent point sources aligned along the optical axis (Fig. 7a). These sources might be thought of as fluorescent beads under illumination by an appropriate pump beam. (A biological equivalent of this object could be a stack of cells in which some of the nuclei are fluorescing.) For the object under consideration, the source locations and intensities are z_k and I_k ($k = 1 \ldots N$), respectively. The distance between two successive samples is a constant Δz. In this section, we compare three alternative imaging systems that can be used to image the sources (i.e. to determine the values of I_k).

A combination of objective–collector lenses (or objective lens and volume hologram) is used in tandem to take *N* measurements $\tilde{I}_j$ ($j = 1 \ldots N$) as follows: at measurement *j*, the objective collimates the pump illumination towards the object sources of interest. This system is, strictly speaking, non-confocal on the illumination side.

The first imaging system (pinhole-based) is shown in Figure 7b. As the objective focuses pump illumination onto source $k = j$, the same source is simultaneously also at the front focus of the collector

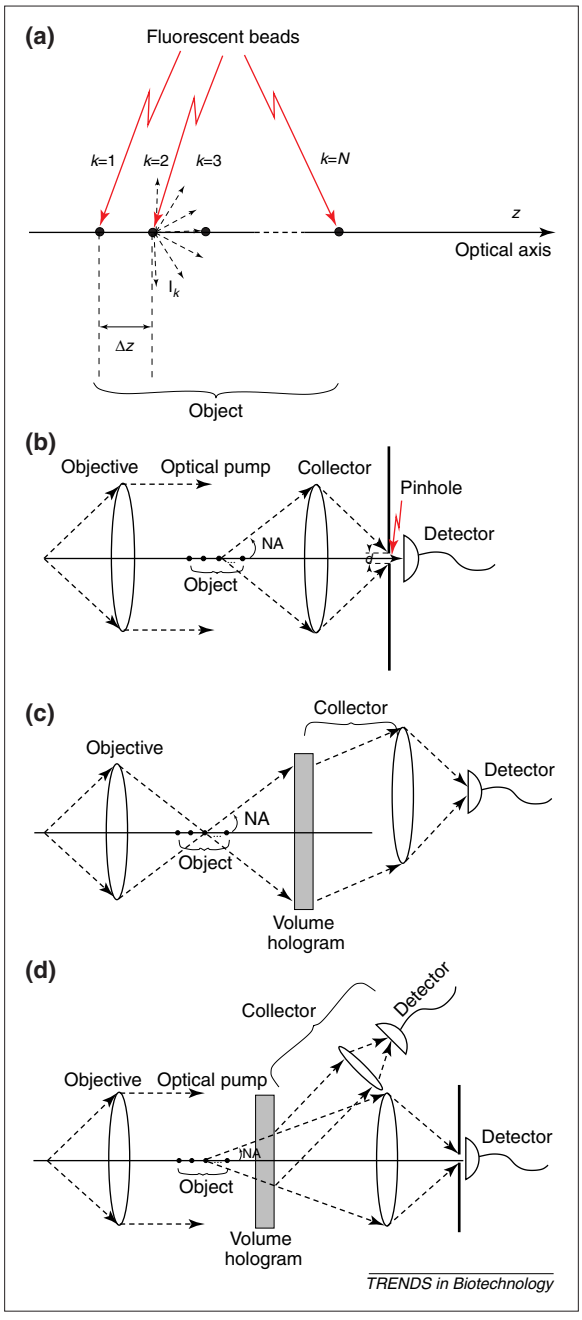

Fig. 7. (a) Source geometry for the simulations. (b) Fluorescence imaging geometry with a lens and a pinhole for depth resolution. (c) Geometry of fluorescence imaging with a volume holographic element. (d) Imaging with a volume holographic element exploiting the undiffracted beam in parallel with the pinhole-based system.

lens. The measurement itself corresponds to the integrated intensity captured by a detector placed behind a pinhole of diameter d. The numerical aperture of the imaging systems is NA and, for notational simplicity, it is assumed that the magnification equals 1 on both sides.

The second system (Fig. 7c) is illuminated similarly except that the collector–pinhole combination has been replaced by a composite collector element made of a volume hologram and a Fourier lens in tandem, and there is no pinhole. (In practice, of course, care has to be taken that light going straight through the hologram does not reach the detector.) The radii of the hologram and the Fourier lens are such that the numerical aperture NA is the same as in the previous system.

The third system (Fig. 7d) is, in a sense, a combination of the previous two systems. The collector lens and pinhole placed after the volume hologram use the light that passes straight through the hologram without being diffracted, as described by the pinhole-based imaging system. Thus, redundant information is obtained about the object from both the hologram and collector lens, and no power is wasted on the collector optics side.

Pinhole-based microscope model

The intensity contributed by source k to measurement j depends on the location of that source relative to the common focal plane of the collector. Large displacements relative to the collector reduce the amount of fluorescence that the pinhole allows to reach the detector.

To simplify the notation later, the normalized pinhole diameter is defined by Eqn 24.

$$\upsilon = \frac{2\pi(\mathrm{NA})d}{\lambda} \qquad [24]$$

Using this definition, the amount of fluorescent power received by the detector per unit of fluorescence emitted by the bead is given by Eqn 25,

$$\underline{\mathbf{H}}^{(\mathrm{lp})}_{jk} = \int_0^{\upsilon_d} \left|L(u,\upsilon)\right|^2 \upsilon \mathrm{d}\upsilon \qquad [25]$$

where u is the normalized longitudinal coordinate (Eqn 26).

$$u = \frac{2\pi(\mathrm{NA})^2 z_{p,k}}{\lambda} \qquad [26]$$

The integral in Eqn 25 is computed[29] in terms of a series expansion, which significantly accelerates the numerical calculations. Notice that the matrix $\underline{\mathbf{H}}^{(\mathrm{lp})}$ is Toeplitz matrix. Therefore, its eigenvalues can be computed more efficiently by a Fourier transformation for large objects.

Volume hologram model

Each element of the system matrix of the volume holographic system is given by the surface integral of the volume-diffracted intensity (Eqn 22) over the entire detector area (because there is no pinhole). To emphasize the lack of a pinhole, the expression for the power measured by the detector is expressed as Eqn 27.

$$\underline{\mathbf{H}}^{(\mathrm{vh})}_{jk} = \varsigma \int\int_{-\infty}^{+\infty} \left| \int_{-L/2}^{L/2} \exp\{i\,\pi C(z)\} \right.$$
$$\left. f(2\pi A(z)R^2, 2\pi B(z)R)\mathrm{d}z \right|^2 \mathrm{d}x'\mathrm{d}y' \qquad [27]$$

The coefficients $A(z)$, $B(z)$ and $C(z)$ computed using Eqns 16–20 using $z_{\mathrm{p},k} = z_k$ and $x_{\mathrm{p},k} = y_{\mathrm{p},k} = 0$. Lacking an analytical expression for the integral in Eqn 27, the values of $\underline{\mathbf{H}}^{(\mathrm{vh})}_{jk}$ are computed by numerical integration. Also, notice that the system

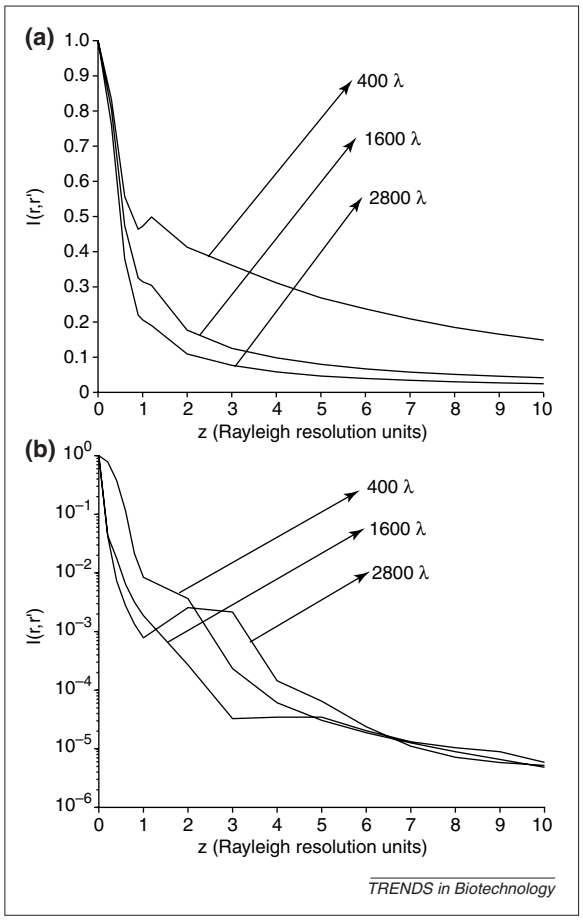

Fig. 8. Integrated intensity (over an infinite detector area) for the volume holographic imaging system of Figure 7c. The hologram has $u = 0.4$, $R = 1500\ \lambda$ and (a) $\mathbf{r}_f = (0, 0, -10^4\ \lambda)$ (on-axis hologram) or (b) $\mathbf{r}_f = (4 \times 10^3\ \lambda, 0, -10^4\ \lambda)$ (off-axis hologram). Results for three different volume-hologram thicknesses are shown.

matrix for the volume hologram only approximates a Toeplitz matrix. Some numerical examples are shown in Figure 8.

Combined model

The dual imaging system of Fig. 7d acquires information through both the volume hologram and a lens-plus-pinhole system. To model the IMI, the observation vectors and system matrices of the individual systems are concatenated (Eqn 28),

$$\begin{pmatrix} \underline{\tilde{I}}^{(\mathrm{lp})} \\ \cdots \\ \underline{\tilde{I}}^{(\mathrm{vh})} \end{pmatrix} = \begin{pmatrix} (1-\eta)\underline{\mathbf{H}}^{(\mathrm{lp})} \\ \cdots \\ \underline{\mathbf{H}}^{(\mathrm{vh})} \end{pmatrix} (\underline{I}) \qquad [28]$$

in which the matrices $\underline{\mathbf{H}}^{(\mathrm{lp})}$ and $\underline{\mathbf{H}}^{(\mathrm{vh})}$ are given by Eqns 25 and 27, respectively. The IMI is computed according to Eqn 8, in which the μ_n terms are the singular values of the concatenated matrix, as mentioned previously. As shown in the next section, the over-determined system of Eqn 28 can be richer or poorer in information return than the individual imaging systems composing it, depending on the value of η.

Numerical comparison

We simulated the imaging performance of the pinhole-based system, the volume-holographic system and their combination by computing the IMI for an object as shown in Fig. 7a with $N = 11$, $\Delta z = 1$ Rayleigh unit $= 2\lambda \div (\mathrm{NA})^2$ and $\mathrm{NA} = 0.15$. To facilitate the interpretation of the results, the fundamental sources of information loss in the two individual optical systems need to be emphasized. In the pinhole-based system, information is lost because of the mismatch between the shape of the point-spread function of the lens and the abrupt discontinuity introduced by the pinhole. When the pinhole diameter d is very small, the information loss shows itself as loss of optical power, which drives down the IMI. However, if the pinhole is opened up too much, it begins to approach a wide-field system with no depth-resolution ability whatsoever. Therefore, the IMI as function of d peaks at an optimum diameter (Fig. 9). Notice that the optimum IMI occurs at a diameter slightly smaller than the lateral Rayleigh resolution limit, which in this case is $1.21\ \lambda \div \mathrm{NA} = 8.1\ \lambda$.

The volume hologram is, by construction, a matched filter (for example, compare Eqns 9 and 13). However, the hologram still loses information because it only diffracts a fraction η of the incident power. The implication is made clear by comparing the data in Fig. 9a, in which the hologram was assumed to have $\eta = 1$, and Fig. 9b, in which the hologram had the more realistic (but still overly optimistic) value $\eta = 0.5$. An ideal hologram ($\eta = 1$) of reasonable thickness (>1000 λ, approximately) outperforms the IMI of the pinhole-based system. This superiority is lost when the diffraction efficiency is limited.

The trade-off between matched filtering and diffraction efficiency from the point of view of the hologram, and pinhole diameter from the point of view of the lens, is further elucidated by considering the combined system of Figure 7d. The IMI of the combined system as function of η for various pinhole diameters and holographic geometries is plotted in Figure 10. When the pinhole-based system is operating at optimum diameter (~6 λ), the use of the hologram in parallel makes sense only at very high diffraction efficiencies. This is shown by the dip in the IMI curves at intermediate η values and is due to the inefficient use of optical power at these regimes. By contrast, when the pinhole is operated at large diameters (e.g. because of geometrical aberrations in the system), the matched-filter operation of the hologram consistently improves imaging performance, even at low diffraction efficiencies. Also, notice that increasing the hologram thickness generally improves the IMI (Fig. 9).

Conclusions

These simulations are intended as demonstrations of the potential of volume holograms for imaging. Despite several approximations (e.g. ignoring lateral object structure, sampling implemented as isolated, mutually incoherent point sources, Gaussian noise

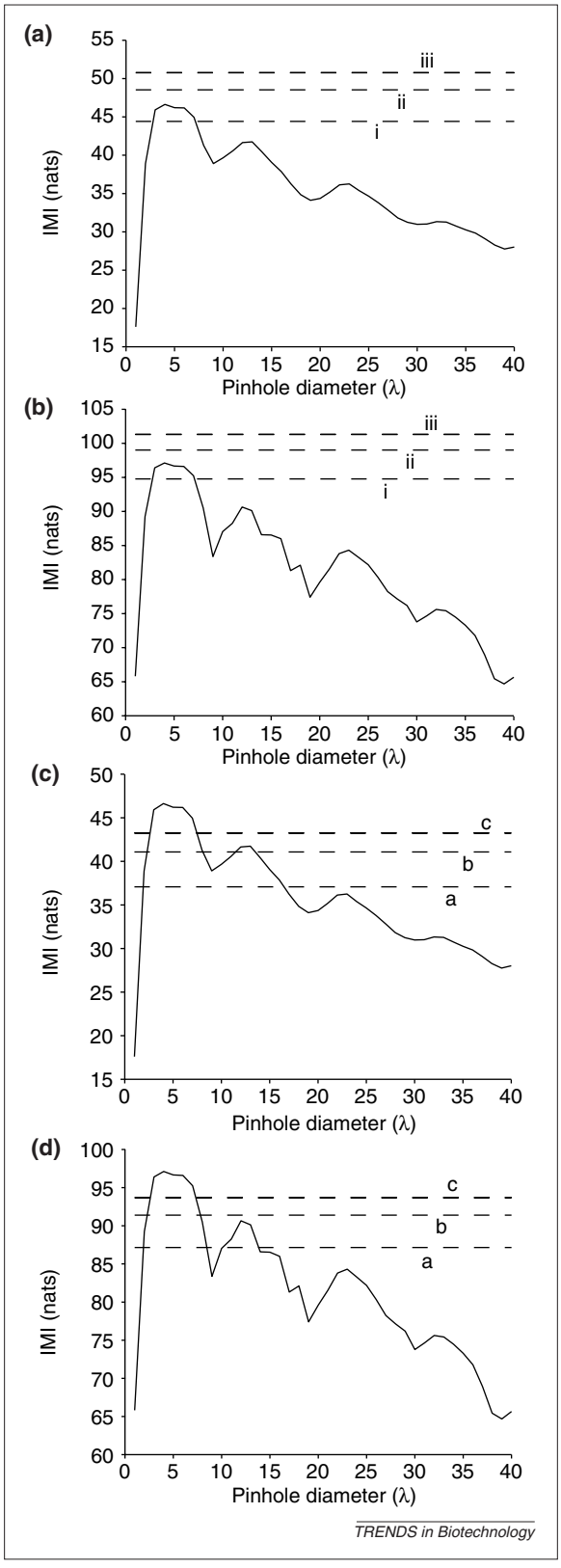

Fig. 9. Comparison of imaging mutual information (IMI) for the imaging system using a lens plus a pinhole of varying diameter (Fig. 7b) with that of a volume hologram (Fig. 7c). The solid line is the IMI of the confocal system and the dashed lines are IMI of various volume holograms. The two plots are for (a) SNR = 10; (b) SNR = 100. Here, the holograms are assumed to be ideal (i.e. to have diffraction efficiency $\eta = 1$). The hologram data are labeled as follows: (i) 400 λ-thick hologram recorded with an on-axis reference $\mathbf{r}_f = (0, 0, -10^4\,\lambda)$, plane-wave signal with $u = 0.4$; (ii) 1600 λ-thick hologram recorded with an on-axis reference $\mathbf{r}_f = (0, 0, -10^4\,\lambda)$, plane-wave signal with $u = 0.4$; and (iii) 400 λ-thick hologram recorded with an off-axis reference $\mathbf{r}_f = (4 \times 10^3\,\lambda; 0, -10^4\,\lambda)$, plane-wave signal with $u = 0.4$. Increasing the thickness to 1600 λ in the off-axis geometry leads only to marginal increase in IMI.

Acknowledgements
Our work was supported by a National Science Foundation CAREER Award to G. Barbastathis, a d'Arbeloff Graduate Fellowship to A. Sinha and the Air Force Research Laboratories (Eglin AFB). We are grateful to W. Liu, D. Psaltis, M. Balberg, D.L. Marks, M.A. Neifeld and D.J. Brady for helpful discussions and suggestions.

statistics), the IMI model provides a convenient tool for understanding trade-offs between light efficiency and resolution. This is particularly appropriate for volume-holographic imaging instruments, in which the advantage of matched filtering is offset by the limited diffraction efficiency.

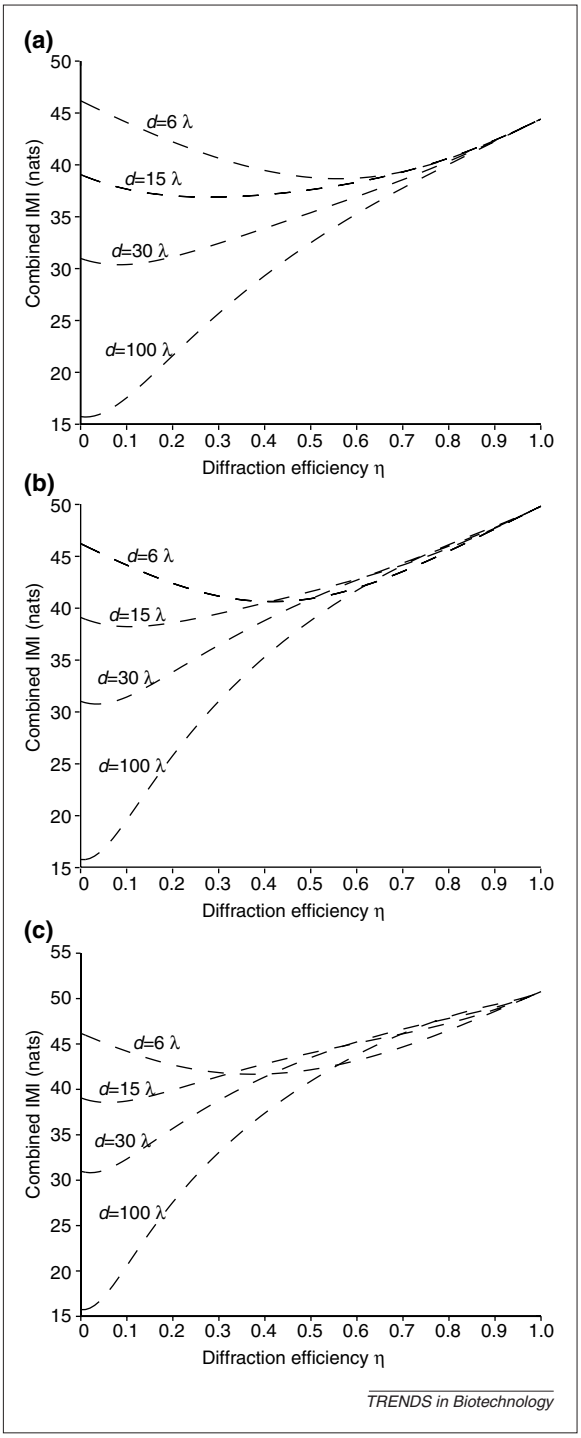

Fig. 10. Imaging mutual information (IMI) for the combined imaging system of Fig. 7d using different pinhole diameters (*d*). The volume holographic geometries considered are: (a) on-axis $\mathbf{r}_f = (0, 0, -10^4\,\lambda)$ with a thickness of 400 λ; (b) on-axis $\mathbf{r}_f = (0, 0, -10^4\,\lambda)$ with a thickness of 2800 λ; and (c) off-axis $\mathbf{r}_f = (4 \times 10^3\,\lambda, 0, -10^4\,\lambda)$ with a thickness of 2800 λ.

Volume holograms can be useful in many imaging contexts, such as spectral imaging and imaging through strongly aberrating media[30]. Experimental demonstrations in spectral microscopy and far-field imaging are currently under way in our laboratory. Compared with other applications of volume holography (e.g. optical memories), in imaging, it is easier to design and

program the hologram. Optimizing the IMI metric (equivalently, optimizing the eigenvalue spectrum of the system's **H** matrix) can serve as a useful design guideline and comparison metric against competing techniques. Finally, a volume hologram is the most appropriate implementation of analog front ends of hybrid imaging systems with digital post-processing[6]. These systems can realize the full range of information extraction predicted by the IMI metric.

References

1 Shannon, C.E. (1948) *Bell Syst. Tech. J.* 27, 379–423
2 Shannon, C.E. (1948) *Bell Syst. Tech. J.* 27, 623–656
3 Di Francia, G.T. (1969) *J. Opt. Soc. Am.* 59, 799–804
4 Frieden, B.R. (1970) Information, and the restorability of images. *J. Opt. Soc. Am.* 60, 575–576
5 Barbastathis, G. *et al.* (1999) Confocal microscopy with a volume holographic filter. *Opt. Lett.* 24, 811–813
6 Barbastathis, G. and Brady, D.J. (1999) Multidimensional tomographic imaging using volume holography. *Proc. IEEE* 87, 2098–2120
7 Minsky, M. (1961) Microscopy apparatus. US Patent 3,013,467
8 Wilson, T., ed. (1990) *Confocal Microscopy*, Academic Press
9 Huang, D. *et al.* (1991) Optical coherence tomography. *Science* 254, 1178–1181
10 Bracewell, R.N. Radio astronomy techniques. In *Encyclopaedia of Physics* (Vol. 54) (Flugge, S., ed.), pp. 159, Springer-Verlag
11 Carter, W.H. and Wolf, E. (1981) Correlation theory of wavefields generated by fluctuating, three-dimensional, primary, scalar sources. I. General theory. *Opt. Acta* 28, 227–244
12 Itoh, K. and Ohtsuka, Y. (1986) Fourier-transform spectral imaging: retrieval of source information from three dimensional spatial coherence. *J. Opt. Soc. Am. A* 3, 94–100
13 Rosen, J. and Yariv, A. (1996) General theorem of spatial coherence: application to three-dimensional imaging. *J. Opt. Soc. Am. A* 13, 2091–2095
14 Marks, D.L. *et al.* (1999) Visible cone-beam tomography with a lensless interferometric camera. *Science* 284, 2164–2166
15 Marks, D. *et al.* (1999) Three-dimensional coherence imaging in the Fresnel domain. *Appl. Opt.* 38, 1332–1342
16 Yang, G.G. *et al.* (2000) Volume reflection holographic confocal imaging. *Appl. Opt.* 39, 4076–4079
17 Li, H.Y.S. *et al.* (1993) Optical network for real-time face recognition. *Appl. Opt.* 32, 5026–5035
18 Levene, M. *et al.* (1999) Method for controlling the shift invariance of optical correlators. *Appl. Opt.* 38, 394–398
19 Leith, E.N. *et al.* (1966) Holographic data storage in three-dimensional media. *Appl. Opt.* 5, 1303–1311
20 Barbastathis, G. *et al.* (1996) Shift multiplexing with spherical reference waves. *Appl. Opt.* 35, 2403–2417
21 Bertero, M. and Boccacci, P. (1998) *Introduction to Inverse Problems in Imaging*, Institute of Physics
22 Slepian, D. (1958) *Bell Syst. Tech. J.* 37, 163
23 Barrett, H.H. (1995) Objective assessment of image quality. II. Fisher information, Fourier crosstalk, and figures of merit for task performance. *J. Opt. Soc. Am. A* 12, 834–852
24 Barrett, H.H. and Smith, W.E. (1986) Hotelling trace criterion as a figure of merit for the optimization of imaging systems. *J. Opt. Soc. Am. A* 3, 717–725
25 Cover, T.M. and Thomas, J.A. (1991) *Elements of Information Theory*, J.W. Wiley
26 Coufal, H. *et al.*, eds (2000) *Holographic Data Storage*, Springer
27 Born, M. and Wolf, E. (1980) *Principles of Optics* (6th edn), Pergamon Press
28 Barbastathis, G. and Psaltis, D. (1996) Shift-multiplexed holographic memory using the two-lambda method. *Opt. Lett.* 21, 429–431
29 Born, M. and Wolf, E. (1998) *Principles of Optics* (7th edn), pp. 492–494, Pergamon Press
30 Balberg, M. (2000) Confocal imaging through scattering media with a volume holographic filter. *Proc. SPIE* 3919, 69–74